JOURNAL OF THE AMERICAN CHEMICAL SOCIETY

Subscriber access provided by Murdoch University Library

Article

Integrating Suitable Linkage of Covalent Organic Frameworks into Covalently Bridged Inorganic/Organic Hybrids toward Efficient Photocatalysis

hou Wang, Cheng Qian, Jia Liu, Yongfei Zeng, Dongdong Wang,
WEIQIANG ZHOU, Long Gu, Hongwei Wu, Guofeng Liu, and Yanli Zhao

J. Am. Chem. Soc., **Just Accepted Manuscript** • DOI: 10.1021/jacs.0c00054 • Publication Date (Web): 19 Feb 2020

Downloaded from pubs.acs.org on February 19, 2020

Just Accepted

"Just Accepted" manuscripts have been peer-reviewed and accepted for publication. They are posted online prior to technical editing, formatting for publication and author proofing. The American Chemical Society provides "Just Accepted" as a service to the research community to expedite the dissemination of scientific material as soon as possible after acceptance. "Just Accepted" manuscripts appear in full in PDF format accompanied by an HTML abstract. "Just Accepted" manuscripts have been fully peer reviewed, but should not be considered the official version of record. They are citable by the Digital Object Identifier (DOI®). "Just Accepted" is an optional service offered to authors. Therefore, the "Just Accepted" Web site may not include all articles that will be published in the journal. After a manuscript is technically edited and formatted, it will be removed from the "Just Accepted" Web site and published as an ASAP article. Note that technical editing may introduce minor changes to the manuscript text and/or graphics which could affect content, and all legal disclaimers and ethical guidelines that apply to the journal pertain. ACS cannot be held responsible for errors or consequences arising from the use of information contained in these "Just Accepted" manuscripts.

is published by the American Chemical Society. 1155 Sixteenth Street N.W., Washington, DC 20036
Published by American Chemical Society. Copyright © American Chemical Society. However, no copyright claim is made to original U.S. Government works, or works produced by employees of any Commonwealth realm Crown government in the course of their duties.

Integrating Suitable Linkage of Covalent Organic Frameworks into Covalently Bridged Inorganic/Organic Hybrids toward Efficient Photocatalysis

Hou Wang,[†⊥] Cheng Qian,[†⊥] Jia Liu,[‡] Yongfei Zeng,[§] Dongdong Wang,[†] Weiqiang Zhou,[†] Long Gu,[†] Hongwei Wu,[†] Guofeng Liu,[†] Yanli Zhao[†,*]

[†]Division of Chemistry and Biological Chemistry, School of Physical and Mathematical Sciences, Nanyang Technological University, 21 Nanyang Link, Singapore 637371, Singapore.

[‡]Department of Chemistry, School of Science, Tianjin University, Tianjin 300072, China

[§]College of Chemistry, Tianjin Normal University, Tianjin 300387, China

ABSTRACT: Covalent organic frameworks (COFs) are excellent platforms with tailored functionalities in photocatalysis. There are still challenges in increasing photochemical performance of COFs. Therefore, we designed and prepared a series of COFs for photocatalytic hydrogen generation. Varying different ratios of β-ketoenamine to imine moieties in the linkages could differ the ordered structure, visible light harvesting and bandgap. Overall β-ketoenamine linked-COFs exhibited much better photocatalytic activity than those COFs having both β-ketoenamine and imine moieties on account of non-quenched excited-state and more favorable HOMO level in photoinduced oxidation reaction from the former. Specifically, after *in situ* growth of β-ketoenamine linked COFs onto NH_2-$Ti_3C_2T_x$ (T_x = -O and -OH) MXene *via* covalent connection, the hetero-hybrid showed an obvious improvement in photocatalytic H_2 evolution because of strong covalent coupling, electrical conductivity and efficient charge transfer. This integrated linkage evolution and covalent hybridization approach advances the development of COF-based photocatalysts.

INTRODUCTION

Covalent organic frameworks (COFs), comprised of purely organic building blocks linked *via* robustly covalent bonds, allow atomically precise integration of organic units into extended two dimensional (2D) or 3D structures with periodic skeletons and ordered nanopores.[1-6] COFs provide tunable platforms in skeletons for the mechanistic studies of correlated organic π systems with exceptionally electronic properties.[7] They have attracted wide attention in semiconductors,[8,9] sensors,[10] catalysis,[11-16] and energy conversion.[17]

Linkage chemistry is an important aspect to COFs in respect to their practicability in optoelectronics or electrochemical applications. Imine or keto-enamine linkages with good electronic communication across the bond have been extensively used in the construction of COFs.[18] Heterostructurally mixed linkage approach significantly increases the structural complexity, functionality and topological diversity from relatively simple building blocks.[19-21] The crystallinity, porosity and active sites of COFs are subsequently changed.[20] Therefore, understanding the correlation between suitable linkages of COFs and efficient photocatalysis is prerequisite but challenging.

Unfortunately, most of pure COF photocatalysts have relatively low photocatalytic efficiency on account of fast charge recombination. Hybridization provides a feasible strategy to improve the charge-carrier separation in photoredox process.[22] So far, photoactive COF-based hybrids are classified into COFs/metal organic frameworks (MOFs),[23-25] COFs/molecular (or single site) catalysts,[26-28] COFs/metal nanoparticles,[29] and COFs/metal sulfides.[30] To the best of our knowledge, there is no report on exploring the covalent connection of COFs with MXene for photocatalysis. MXene, a group of 2D transition metal nitrides/carbides/carbonitrides, shows many promising properties such as charge mobility anisotropy, metallic conductivity, and tunable surface-terminated chemistry (-O, $-NH_2$, -F, -OH, etc).[31-34] It could be envisioned that the covalent bond bridged hybrid is not only beneficial to optoelectronics (for instance, photogenerated electron transfer) between 2D MXene and COFs, but also maximally allows the exposure of active sites. The porous structure also favors for the mass transfer and facilitates the substrates to access the active sites of catalysts.

Herein, we synthesized three kinds of COFs with various ratios of β-ketoenamine to imine moieties by acid-catalyzed Schiff-base reaction of benzene-1,4-diamine (BDA) with benzene-1,3,5-tricarbaldehyde derivatives bearing different numbers of hydroxy groups (Scheme 1). More ordered COFs benefit from the compromised outcome of conformational pre-organization between the planar keto-enamine moieties (irreversible) and the twisted imine of linkage (reversible) in periodic frameworks, visible light harvesting and photoredox capacity. The more β-ketoenamine moiety is, the higher photocatalytic performance shows, on account of favorable highest occupied molecular orbital (HOMO) energy level for photoinduced oxidation reaction. The excited state of mixed-linkages is suppressed by the imine moiety in the presented

Scheme 1. Schematic illustration for the synthesis of *β*-ketoenamine linked COFs and hybridization with NH_2-MXene.

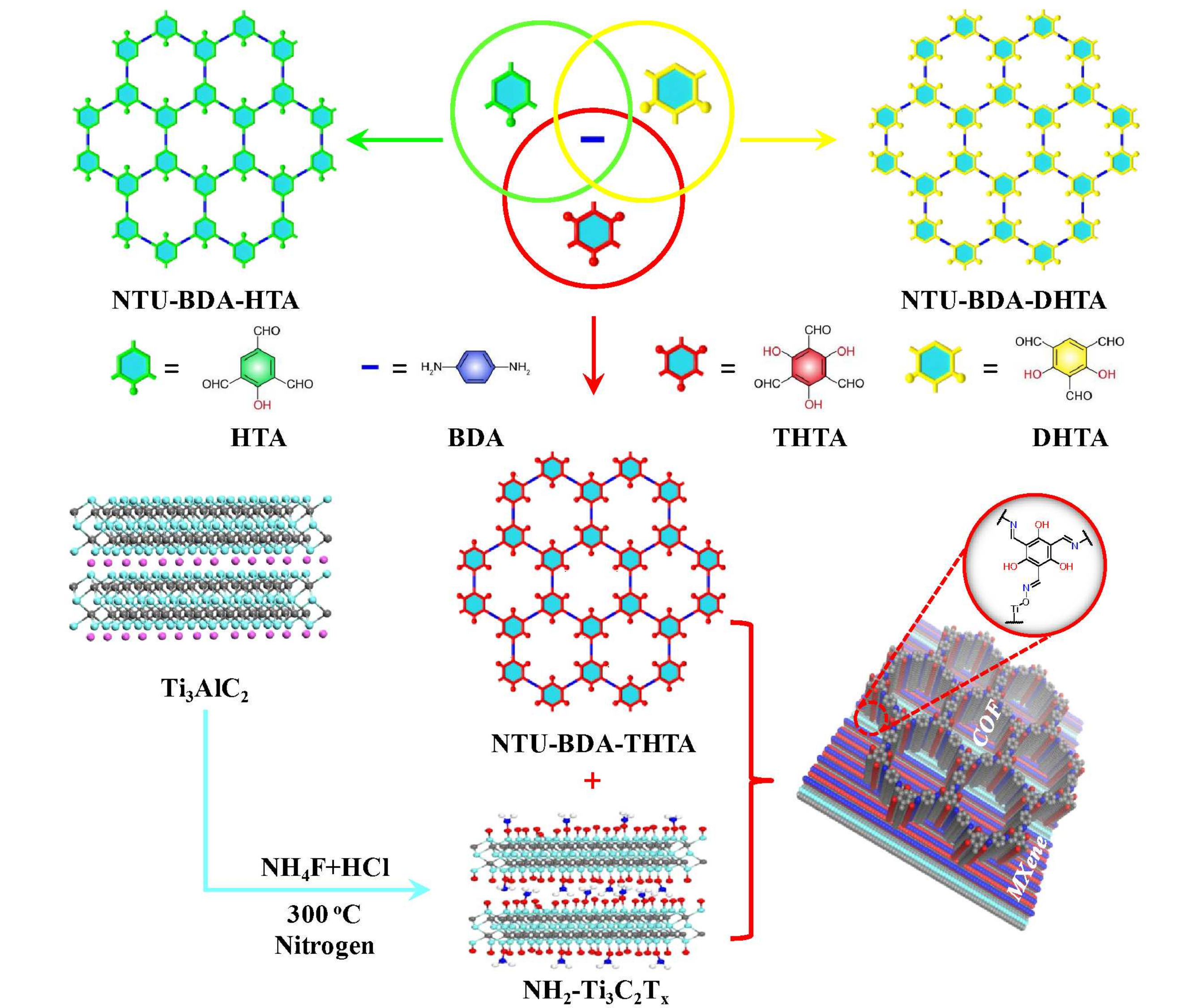

Scheme 2. Various ratios of *β*-ketoenamine (orange) to imine (blue) moieties in the unit cell of COFs: (a) NTU-BDA-HTA (2:4), (b) NTU-BDA-DHTA (4:2), and (c) NTU-BDA-THTA (6:0).

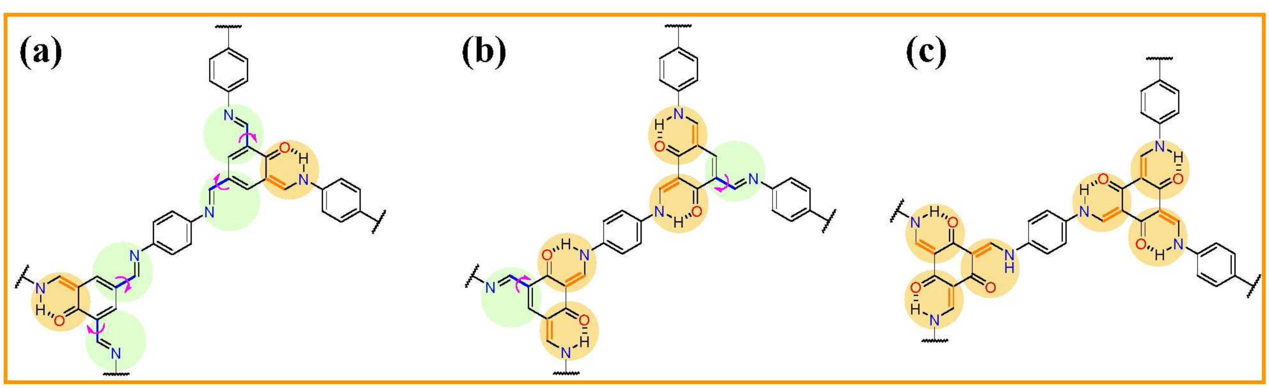

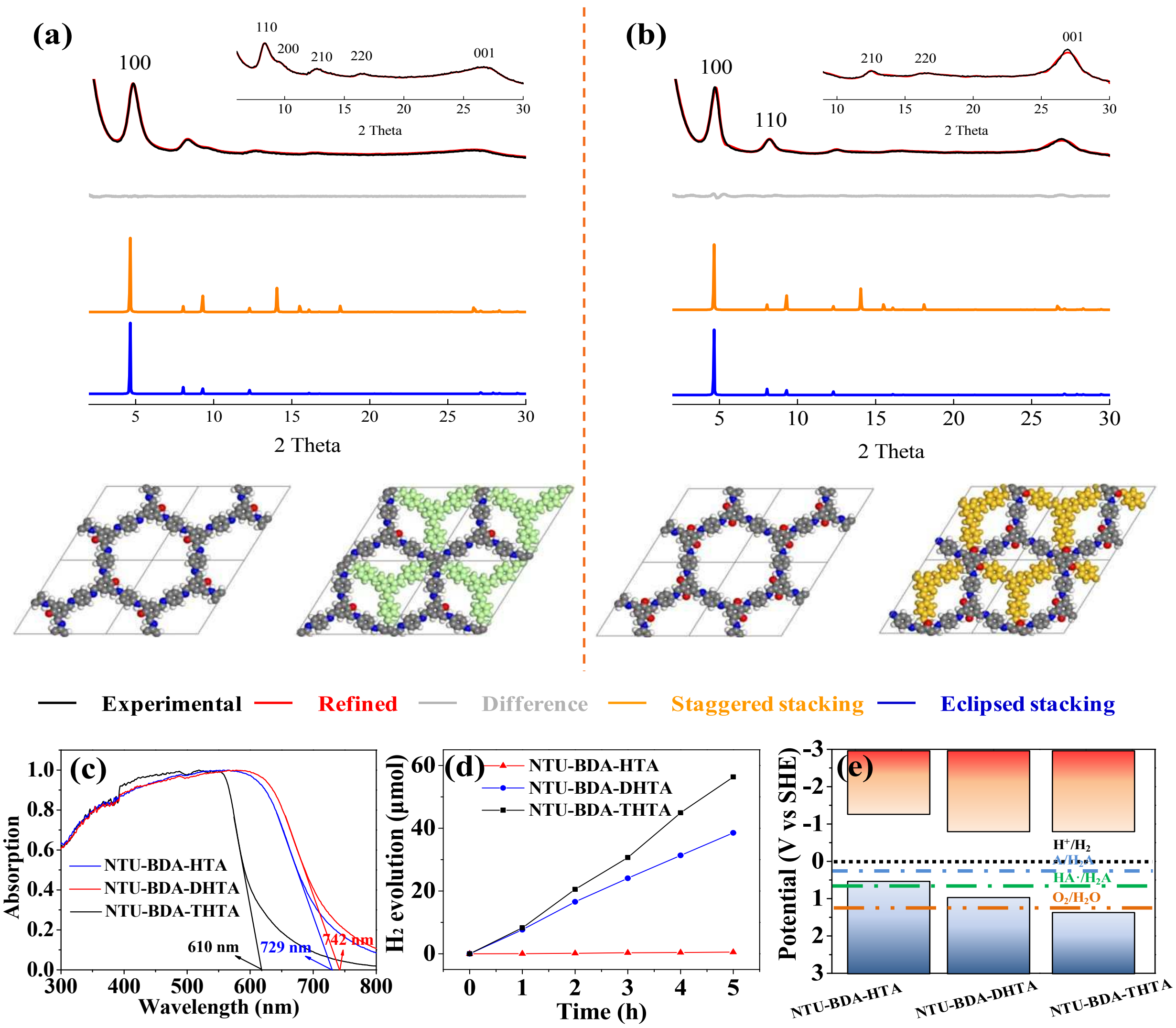

Figure 1. Experimental and simulated PXRD patterns for (a) NTU-BDA-HTA and (b) NTU-BDA-DHTA, (c) UV-vis-DRS spectra, (d) photocatalytic H_2 evolution performance, and (e) energy band potentials of these three COFs. Blue and green lines stand for the two-hole (A/H_2A) and one-hole ($HA\bullet/H_2A$) oxidation of *L*-ascorbic acid, respectively.

COFs (NTU-BDA-HTA and NTU-BDA-DHTA) *via* photoinduced electron transfer. Encouraged by the planar structure, moderately ordered structure, non-quenched excited-state and appropriate HOMO energy of NTU-BDA-THTA, covalent coupling with NH_2-$Ti_3C_2T_x$ enables the formation of 2D/2D COF/NH_2-$Ti_3C_2T_x$ hybrids. The hybrids concurrently realize efficient separation and transfer of photogenerated charge carriers for surface proton reduction on account of synergistic effect of heterostructures in photoelectrochemical properties. This method shows a general synthetic applicability to construct more COF/MXene hybrids for the photocatalysis.

RESULTS AND DISCUSSION

Understanding intrinsic correlation between linkages of COFs and photocatalysis. Three ordered COFs, *i.e.*, NTU-BDA-HTA, NTU-BDA-DHTA, and NTU-BDA-THTA, were constructed under solvothermal conditions *via* cascade reaction (reversible Schiff base and irreversible tautomerism reaction) of BDA with different aldehyde building blocks including 2-hydroxybenzene-1,3,5-tricarbaldehyde (HTA), 2,4-dihydroxybenzene-1,3,5-tricarbaldehyde (DHTA), and 4,6-trihydroxybenzene-1,3,5-tricarbaldehyde (THTA), respectively (Scheme 2). In order to obtain COFs with the highest order degree of structure, the condensation conditions were thoroughly screened (Tables S1-S3). Crystalline NTU-BDA-HTA and NTU-BDA-DHTA (Figures S1-S3) were produced using a mixture of dioxane/acetic acid (aqueous 6M, 10/1, v/v) and dioxane/mesitylene/acetic acid (aqueous 3M, 5/5/1, v/v/v), respectively. Both are insoluble in water and common organic solvents.

As revealed from powder X-ray diffraction (PXRD) pattern (Figure 1a), NTU-BDA-HTA holds a long-range ordered structure, exhibiting the most intense peak at 4.78° (2θ), which corresponds to the (100) diffraction. Diffraction peaks at 8.41°, 9.65°, 12.69°, 16.45° and 26.64° were also observed, assigned to the (110), (200), (210), (220) and (001) diffraction, respectively. For NTU-BDA-DHTA (Figure 1b), the most intense peak at 4.67° corresponds to the (100) diffraction, with other minor peaks at 8.14°, 12.66°, 16.66° and 27.16° for the (110), (210), (220) and (001) diffraction, respectively. The experimental PXRD patterns (Figure 1a,b) for NTU-BDA-

HTA and NTU-BDA-DHTA matched well with the simulated patterns of the eclipsed stacking (AA) model in the monoclinic system P_2/M space group. Pawley refinement gave the optimized unit cell parameters as follows: a = b = 22.36 Å, c = 3.35 Å, α = β = 90.00° and γ = 122.68°, with R_{wp} = 3.59% and R_p = 2.27% for NTU-BDA-HTA; a = b = 22.50 Å, c = 3.27 Å, α = β = 90.00° and γ = 119.04°, with R_{wp} = 3.85% and R_p = 2.63% for NTU-BDA-DHTA. These results indicate that the two COFs have the predicted frameworks. Fourier transform infrared spectroscopy spectra (Figures S4-S6) and solid ^{13}C cross-polarization magic angle spinning nuclear magnetic resonance spectroscopy (Figures S7 and S8) unambiguously demonstrated the coexistence of *β*-ketoenamine and imine moieties in both NTU-BDA-HTA and NTU-BDA-DHTA.

Scanning electron microscopy (SEM) and transmission electron microscope (TEM) images (Figures S9 and S10) indicate that NTU-BDA-HTA, NTU-BDA-DHTA and NTU-BDA-THTA have urchin-like, microsphere-like and clavate-like morphology with the particle size of above 1 μm, respectively. The domains of straight black-and-white lattice fringes visualize the interplanar spacing of π-π stacking between the adjacent layers in the COFs. Thermogravimetric analyses (Figure S11) and water contact angles results (Figure S12) prove the thermal stability and super-hydrophilic nature, respectively.

N_2 adsorption/desorption (Figure S13) tests reveal the porous features with the pore size of 1.4 nm, close to the theoretical value (Figure S14). The Brunauer-Emmett-Teller (BET) surface areas of NTU-BDA-HTA, NTU-BDA-DHTA and NTU-BDA-THTA is 1289.3, 1344.2 and 768.0 m^2 g^{-1}, respectively. Higher surface area may be due to more long-range ordered skeleton in NTU-BDA-DHTA. The ratio of imine to *β*-ketoenamine influences the order degree of structure in COFs, as verified by normalizing the PXRD intensity (Figure S15). The (100) peak of NTU-BDA-HTA, NTU-BDA-DHTA and NTU-BDA-THTA has a full width at half maximum (FWHM) of 1.00°, 0.79° and 1.42°, respectively. The reported LZU-1 with a FWHM of 1.68° was used as a comparison. According to the Scherrer equation (Supporting Information),[35] the lowest FWHM means that NTU-BDA-DHTA should have the maximum π-conjugated order degree. It can be explained that the single bond (Scheme 2 and Figures S16 and S17) adjacent to imine bond can freely rotate, leading to a variable conformation due to the lack of intramolecular hydrogen bond. Notably, the rotation of backbone moieties is likely kinetically trapped in the bulk.[31] Free rotation of bonds may only occur to imines near the surface, edge, or defects.[36] Thus, the neighboring imine bond can readily undergo the self-correction process. For the special case in NTU-BDA-THTA, the self-correction process can be impeded once the irreversible tautomerization occurs (Figure S17). Theoretical calculations based on the model compounds 1-7 (Figures S18-S21) verify that the totally imine-liked model compound is twisted. The more *β*-ketoenamine form increases, the better planar those model compound shows. Model compound 7 has the most planar structures with the minimum relative energy change (Figure S21). Although the planar structure of NTU-DBA-THTA shown in the framework is from the view of local region, the conjugated extension of long-range ordered structure is limited by the totally irreversible tautomerism (Figure S16). Therefore, more ordered COFs may be resulted from the compromised outcome of conformational pre-organization between the planar *β*-ketoenamine moieties (irreversible) and the twisted imine of linkage (reversible) in periodic frameworks.

Owing to the formation of overall β-ketoenamine linkages through reversible/irreversible tandem reaction, an optical absorbance edge around 610 nm was endowed (Figure 1c) for NTU-BDA-THTA, whereas red shifts to 742 and 729 nm were observed for NTU-BDA-DHTA and NTU-BDA-HTA, respectively. The shift is probably attributed to higher conjugation degree originated from the delocalization along and across the plane in the extended frameworks during the self-repaired and crystallized process.[37] The ratio (4:2) of *β*-ketoenamine to imine linkages simultaneously ensures higher degree of ordered domains and delocalization, leading to the largest red-shifted absorption of NTU-BDA-DHTA. Optical bandgaps (Figure S22) are 1.81, 1.77 and 2.09 eV for NTU-BDA-HTA, NTU-BDA-DHTA and NTU-BDA-THTA, respectively.

Photocatalytic hydrogen evolution was conducted in buffer solution (pH 7.0) under visible light (≥ 420 nm) with Pt and *L*-ascorbic acid as co-catalyst and sacrificial electron donor, respectively. The highest H_2 accumulation amount was obtained from NTU-BDA-THTA, followed by NTU-BDA-DHTA and NTU-BDA-HTA (Figure 1d). Obviously, photocatalytic H_2 evolution rates that were normalized to specific surface area over these three samples also kept the same order (Figure S23), demonstrating the superiority of NTU-BDA-THTA (1.47 μmol h^{-1} m^{-2}). The tendency of photocatalytic H_2 evolution rate differentiates with the PXRD and UV-vis diffuse reflectance spectroscopy (DRS) results, suggesting that the order degree of structure and light-energy absorption of the three COFs are not crucial factors in affecting photocatalytic activity. Photoluminescence spectrum (Figure S24a) shows that the excited state of the mixed linkages is suppressed by the imine moiety in NTU-BDA-HTA and NTU-BDA-DHTA *via* photoinduced electron transfer,[38] which may stymie H_2 production rate. Furthermore, compared with these HOMO and lowest unoccupied molecular orbital (LUMO) potentials from the results of valence X-ray photoelectron spectroscopy (XPS) and Mott-Schottky measurements (Figures 1e, S25 and S26), it can be deduced that more positive potentials of the HOMO energy upon increasing *β*-ketoenamine linkage bring about an increase in the oxidizing power of photogenerated holes, which would be much easier to remove from NTU-BDA-THTA by *L*-ascorbic acid. Efficient hole quenching is possibly achieved by hydrogen bonding interaction with sacrificial donors. Another non-negligible factor is the electron-deficient property of the ketone building block, which may be useful to stabilize the negative charges generated on the COFs and transfer them to the nearby Pt sites. Density functional theory calculations further verify that the *β*-ketoenamine linkage with more O 2p atoms changes the HOMO energy for the enhancement of oxidation performance (Figure 2a,b and S27). In views of industrial applications, the photocatalytic efficiency of pure NTU-BDA-THTA is still far away from practical requirements. The insights obtained from the above results including planar conformation, ordered structure, non-quenched excited state and appropriate HOMO energy in NTU-BDA-THTA provide strong inspiration on post-modification of COF-based materials *via* 2D/2D heterostructures for photocatalysis.

ACS Paragon Plus Environment

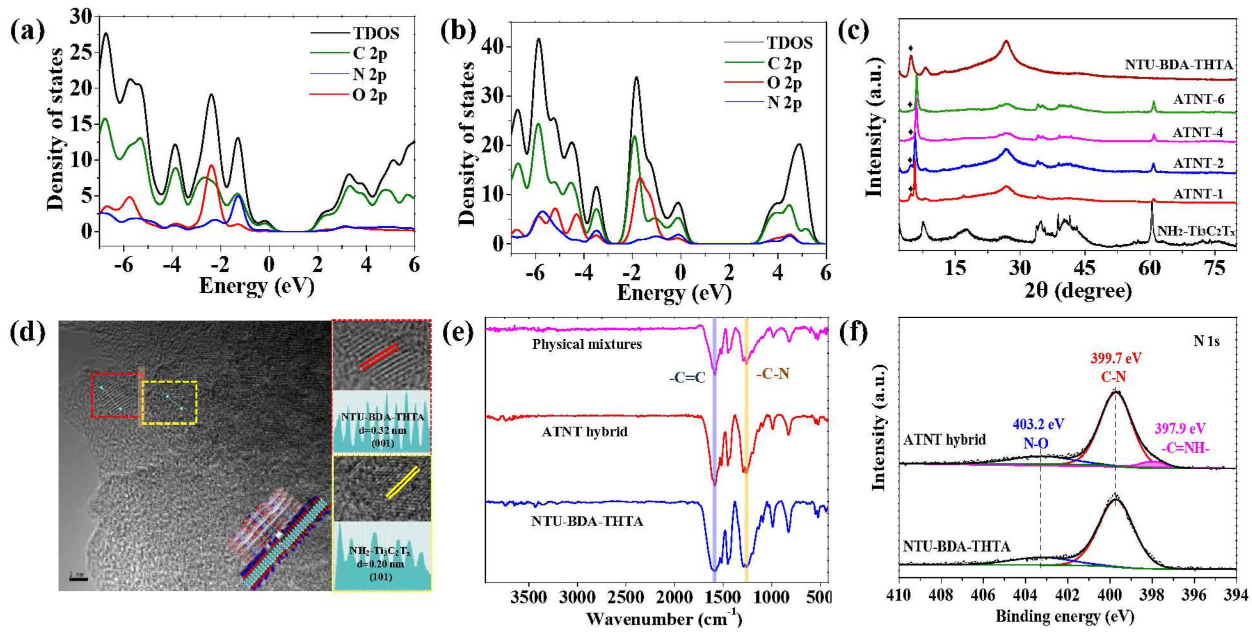

Figure 2. Density of states for (a) NTU-BDA-DHTA and (b) NTU-BDA-DHTA. (c) PXRD patterns of NH_2-$Ti_3C_2T_x$, NTU-BDA-THTA, and ATNT hybrids. (d) HR-TEM image (scale bar: 2 nm) of ATNT-4 with insets of epitaxial orientation between MXene and COF. (e) FT-IR spectra of physical mixture, ATNT hybrid, and NTU-BDA-THTA. (f) N 1s XPS spectra of NTU-BDA-THTA and ATNT hybrid.

Construction and characterization of ATNT hybrids. Successful synthesis from Ti_3AlC_2 and $Ti_3C_2T_x$ to NH_2-$Ti_3C_2T_x$ at various stages was verified by PXRD and SEM results (Figures S28 and S29). NH_2-$Ti_3C_2T_x$ has accordion-like morphology with closely linked and stacked sheets. The energy-dispersive X-ray spectroscopy, Fourier-transform infrared (FT-IR) and XPS analysis (Figures S29e, S30 and S31) of NH_2-$Ti_3C_2T_x$ confirm the elemental composition (Ti, C, N, and O) and the surface termination with N-containing functional groups (-NH_2, O-Ti-N and Ti-O-N). PXRD patterns (Figures 2c and S32) of NTU-BDA-THTA/NH_2-$Ti_3C_2T_x$ (ATNT) hybrids show good consistence with that of respective NTU-BDA-THTA and NH_2-$Ti_3C_2T_x$, demonstrating structural integrity of ordered NTU-BDA-THTA with NH_2-$Ti_3C_2T_x$. Two peaks of ATNT hybrids at 4.76° and 7.66° correspond to the (100) diffraction of NTU-BDA-THTA and (002) diffraction of NH_2-$Ti_3C_2T_x$, respectively. As compared with pure NH_2-$Ti_3C_2T_x$, an apparent shift from 7.66° to 5.65° was observed in ATNT hybrids, indicating the intercalation and delamination of NH_2-$Ti_3C_2T_x$ on account of the presence of NTU-BDA-THTA.[39-41] In situ growth of NTU-BDA-THTA with NH_2-$Ti_3C_2T_x$ provides enough accessible contact surface, as also demonstrated by SEM images (Figures S33 and S34). Compared with smooth surface of pure NH_2-$Ti_3C_2T_x$ (Figures S35a), the NTU-BDA-THTA sticks with sheet-like microstructure are uniformly attached on NH_2-$Ti_3C_2T_x$. High resolution TEM (HR-TEM) image (Figure 2d) of ATNT-4 hybrid shows apparent light-dark lattice fringes with the distance of 0.32 nm and 0.20 nm, corresponding to the (001) and (101) diffractions (Figure S35a,b) of NTU-BDA-THTA and NH_2-$Ti_3C_2T_x$ in the ordered structure, respectively. Combined results from the π-π stacking (001) diffraction of layered NTU-BDA-THTA and less distinct lattice stripes in the interfacial area indicate specific orientation anisotropy between NTU-BDA-THTA and NH_2-$Ti_3C_2T_x$. That is, polymeric NTU-BDA-THTA microcrystals might be in a parallel mode along the (001) direction aligned on NH_2-$Ti_3C_2T_x$.[42] With the assistance of graphene-like NH_2-$Ti_3C_2T_x$ substrate, on-surface-grown NTU-BDA-THTA forms preferentially oriented 2D layers parallel to the substrate surface with vertically aligned π-columns.[43-46]

FT-IR spectrum (Figure 2e) of ATNT hybrid is similar to that of pristine NTU-BDA-THTA, showing that the chemical groups remain. No noticeable shift at 1260.5 cm^{-1} (-C-N- bond) and 1584.3 cm^{-1} (-C=C-) in comparison with the physical mixture was observed. As seen from the N 1s of XPS (Figure 2f), the doublet peak at 399.7 eV and 403.2 eV could be assigned to the C-N and N-O groups in ATNT, respectively.[47] A new peak appears at 397.9 eV for ATNT, corresponding to the imine linkage (-C=NH- bond) originated from the aldehyde-amidogen condensation reaction between the precursor of THTA and the amino group of NH_2-$Ti_3C_2T_x$.[48] A typical signal of carbon from the C=N group was observed at 160 ppm in the ^{13}C CP/MAS NMR spectrum of ATNT (Figure S36),[49] further supporting the formation of heterojunction in covalently bridged hybrids.

The BET surface areas (Figure S37) of ATNT-1, ATNT-2, ATNT-4 and ATNT-6 are 569.3, 683.6, 372.2 and 407.7 $m^2\ g^{-1}$ respectively, which are lower than that of NTU-BDA-THTA (768.0 $m^2\ g^{-1}$) due to the presence of NH_2-$Ti_3C_2T_x$ with a low surface area (0.4 m^2/g, Figure S38). Moreover, all the ATNT hybrids have analogical pore size distribution around 1.4 nm. The thermogravimetric analysis proves that the ATNT hybrids own enhanced thermal stability in comparison with bare NTU-BDA-THTA (Figure S39) due to the thermal-stability and high thermal-conductivity of NH_2-$Ti_3C_2T_x$ and the presence of thermal-stable imine bond in the heterojunction of hybrids.[31,40,49]

Optoelectronic properties and photocatalytic H_2 evolution. Solid UV-vis-DRS (Figure 3a) shows that NH_2-$Ti_3C_2T_x$ has overall light absorbance with no distinct absorption edge in the 300-800 nm range. There is a strong absorption band with a steep edge around 610 nm in visible-light region for NTU-BDA-THTA. The bandgap of ATNT hybrids is still 2.09 eV

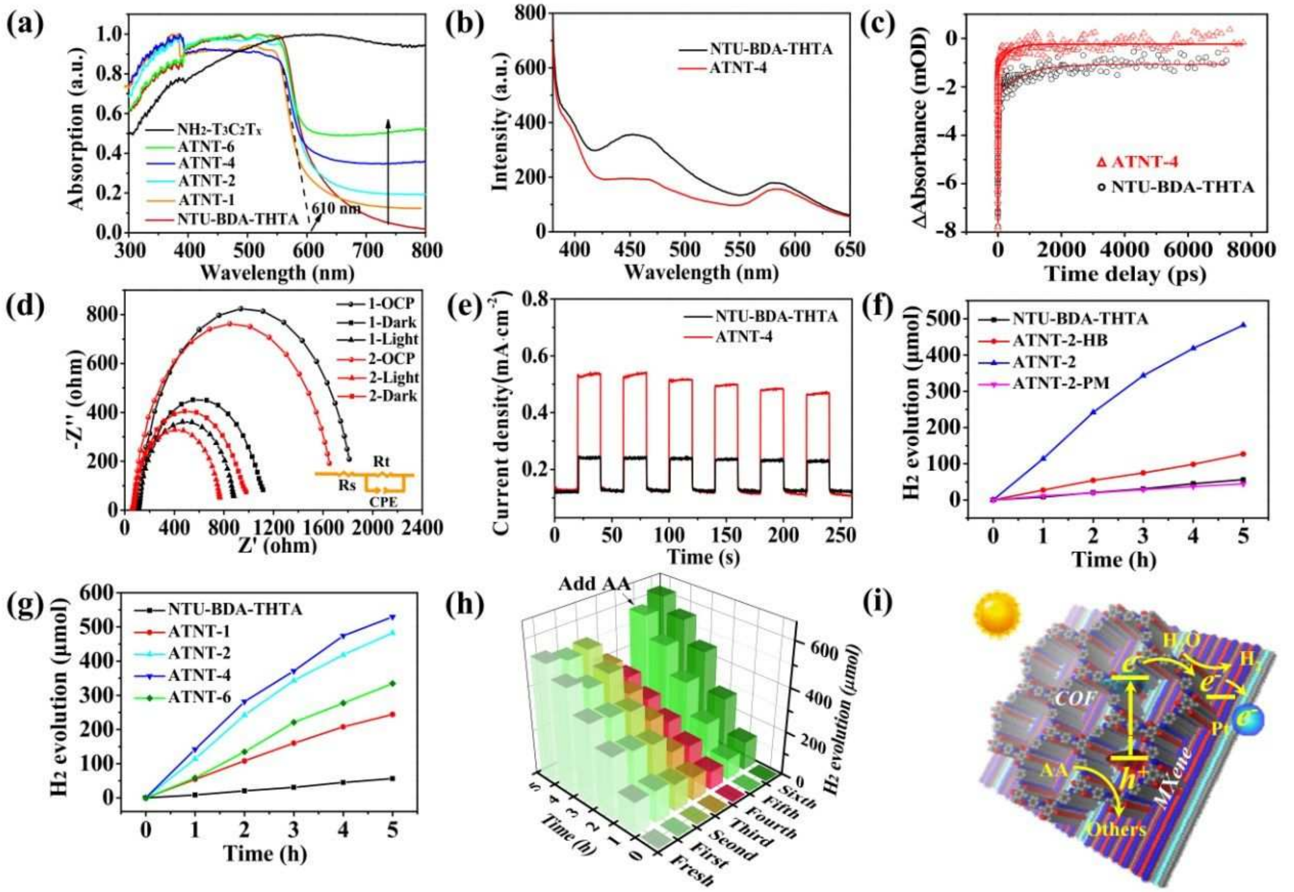

Figure 3. (a) UV-vis-DRS spectra. (b) Steady-state photoluminescent spectra. (c) Transient absorption decay profiles. (d) Electrochemical impedance spectroscopy of 1 (NTU-BDA-THTA) and 2 (ATNT-4) under the conditions of dark, visible light irradiation and open circuit potential (OCP). (e) Transient photocurrent responses. (f) Photocatalytic H_2 evolution comparison between ATNT-2-HB, ATNT-2 and physical mixing material ATNT-2-PM. (g) Photocatalytic H_2 evolution of NTU-BDA-THTA and ATNT hybrids. (h) Recyclability of ATNT-4 for H_2 generation over 30 h. (i) Schematic mechanism of ATNT-4 for photocatalysis.

(Figure S40), indicating that the presence of NH_2-$Ti_3C_2T_x$ has no influence on the band gap of NTU-BDA-THTA. The black NH_2-$Ti_3C_2T_x$ merely increases the absorption baseline with incorporated with distinct adsorption of carbonaceous materials.[50] Electrical conductivity of NH_2-$Ti_3C_2T_x$ are proven by the linear relationship between current and voltage for the NH_2-$Ti_3C_2T_x$ film (Figure S40). Meanwhile, steady-state photoluminescence (PL) spectra in Figure 3b exhibits obvious PL quenching of the ATNT-4 hybrid, in contrast with that of pure NTU-BDA-THTA. The average emission lifetime (Figure S41) displays an obvious increase for ATNT-4 (1.307 ns) as compared with that of bulk NTU-BDA-THTA (0.950 ns), being ascribed to intrinsic deep donor-acceptor states.[51] The PL quenching and prolonged excited state mean the construction of charge transfer channel between NTU-BDA-THTA and NH_2-$Ti_3C_2T_x$ in ATNT, leading to efficient suppression of photoexcited charge recombination and interfacial charge transfer *via* the ATNT heterojunction.

Time-resolved transient absorption spectroscopy (Figures 3c and S42) of TANT-4 exhibits much longer lifetime (or longer-lived charge-separated states) than that of pure NTU-BDA-THTA, suggesting that the incorporation of NH_2-$Ti_3C_2T_x$ inhibits charge recombination in TANT-4.[26] Electrochemical impedance spectrum of ATNT-4 (Figure 3d) exhibits smaller semicircle in the Nyquist plot than that of pure NTU-BDA-THTA, indicating its lower charge transfer resistance (Table S4) that warrants efficient transportation and separation of charge carriers. Transient photocurrent (Figure 3e) of ATNT-4 is clearly stronger than that of NTU-BDA-THTA, indicative of more electron accumulation due to the enhanced charge carrier transfer and electron-hole separation *via* the heterojunction. Linear sweep voltammetry curve of ATNT-4 reveals higher cathodic current density than that of NTU-BDA-THTA (Figure S43), attributed to higher conversion of water to hydrogen over the former. The observed phenomenon clearly indicates that the covalently integration of NTU-BDA-THTA with NH_2-$Ti_3C_2T_x$ not only facilitates the electron separation and extraction, but also accelerates the protonation of H_2O and subsequent H_2 formation.

In photocatalytic H_2 evolution, the presence of Pt or NH_2-$Ti_3C_2T_x$ could improve the H_2 generation rate of NTU-BDA-THTA (Figure S44). The enhanced activity of NH_2-$Ti_3C_2T_x$ is comparable with Pt preloaded NTU-BDA-THTA, proving that NH_2-$Ti_3C_2T_x$ is a possible substitution to noble Pt as the cocatalyst for COFs-based photocatalytic systems. Similar improved photocatalytic performance of metal sulfides using Ti_3C_2 as the cocatalyst has been reported by Qiao *et al*.[52] There was no photocatalytic activity for the pristine NH_2-$Ti_3C_2T_x$ in the presence and absence of platinum (Figure S45). Interestingly, the co-presence of Pt and NH_2-$Ti_3C_2T_x$ enormously improves the efficiency of photocatalytic H_2 evolution. The effect of different connection ways (*i.e.*, covalent, noncovalent and physical mixture) in hybrids was then explored for photocatalytic H_2 generation. As shown in Figures 3f and S46, cumulative H_2 production increases with time, where the case of ATNT-2 increases much faster in comparison with the bare NTU-BDA-THTA. Meanwhile, the photocatalytic activity of ATNT-2 with the covalence connection is 4.2 and 10.38 times higher than that of ATNT-2-HB (with noncovalent connection) and ATNT-2-PM (physical mixing between NTU-BDA-THTA and NH_2-$Ti_3C_2T_x$), clearly confirming the prominent role of covalent bonds between NTU-BDA-THTA and NH_2-$Ti_3C_2T_x$ *via* the heterojunction in improving the photocatalytic activity.

The relationship between component proportions and photocatalytic activity was optimized (Figures 3g and S47). Photocatalytic performance was significantly enhanced upon coupling NTU-BDA-THTA with NH_2-$Ti_3C_2T_x$, as evidenced by the increase of H_2 production with increasing the NH_2-$Ti_3C_2T_x$ content, achieving the maximum of 14,228.1 μmol g^{-1} h^{-1} at the mass ratio of 8:4 (NTU-BDA-THTA : NH_2-$Ti_3C_2T_x$). This value is about 12.6 times higher than that of pure NTU-BDA-THTA (1,127.1 μmol g^{-1} h^{-1}). After normalizing to specific surface area over these samples, the photocatalytic H_2 evolution rate also kept the same order (Figure S48), excluding the mass transfer effect. The improvement is again due to the heterojunction in ATNT hybrids with preferred charge transfer pathway *via* synergistic effect of photoactive NTU-BDA-THTA and conductive NH_2-$Ti_3C_2T_x$. Photocatalytic H_2 generation rate of ATNT-4 is also comparable to that of other recent reports (Table S5). The apparent quantum efficiency (AQY) of 7.75% and 9.75% was determined for ATNT-4 at 420 nm and 500 nm, respectively (Figure S49). These values exceed the AQY of most COF-based photocatalysts reported so far, such as sulfone-containing FS-COF (AQY_{420nm} = 3.2%),[53] g-$C_{40}N_3$–COF (AQY_{420nm} = 4.48%),[54] triazine-based N_3-COF (AQY_{420nm} = 0.44%),[37] g-$C_{18}N_3$–COF (AQY_{420nm} = 1.06%),[55] and TpDTz COF-NiME (a Ni-thiolate COF cluster, AQY_{400nm} = 0.2%).[56] Significantly, a further increase of the NH_2-$Ti_3C_2T_x$ content results in the decreased H_2 production on account of shielded light absorption and blocked active sites by the redundant NH_2-$Ti_3C_2T_x$. Therefore, the NH_2-$Ti_3C_2T_x$ amount was optimized to obtain the best H_2 production. Accordingly, ATNT-4 still retains its original photocatalytic activity after six cycles over 30 h (Figure 3h). No obvious difference in PXRD patterns (Figure S50) and morphology (Figure S51) was observed before and after the six cycles of photocatalysis. These analyses indicate that ATNT-4 presents excellent photocatalytic activity, recyclability, and structural stability. Labeling experiment *via* photocatalytic D_2O splitting to D_2 confirmed that the source of liberated hydrogen was indeed water (Figure S52).

In contrasts to ATNT-4, three kinds of referred materials (Figure S53-S55) including amorphous NTU-BDA-THTA (non-porous), amorphous NTU-BDA-THTA/NH_2-$Ti_3C_2T_x$ hybrid (named amorphous ATNT-4) and model molecule have lower photocatalytic H_2 efficiency. This result indicates that the ordered structure and porous channel of COFs facilitate the exposure of active sites and the mass transfer, which are necessary to achieve efficient photocatalysis. The comparison of photocatalytic H_2 evolution for ATNT-4 at different pH conditions clearly demonstrates that there is largely decreased photocatalytic performance under pH 10.0, while no change is shown under pH 4.0 and 7.0 (Figure S56). The disappearance of the (100) diffraction in the PXRD pattern after the photocatalysis in aqueous solution with pH 10.0 under visible light irradiation indicates that the NTU-BDA-THTA structure in ATNT-4 is destroyed in this condition (Figure S57).

As illustrated in Figure 3i, abundant Pt particles are photo-deposited on the surface of both NTU-BDA-THTA and NH_2-$Ti_3C_2T_x$ sheets to form two-stage cascaded hetero-interfaces among the three components (Figure S58). The NTU-BDA-THTA component with a light-harvest role is photo-induced to form the transition state of HOMO (ground state) → $HOMO_{ex}$, $LUMO_{ex}$ (excited state) upon visible light irradiation. Photogenerated electrons in $HOMO_{ex}$ fleetly transfer to the NH_2-$Ti_3C_2T_x$ component through covalent bond in heterojunction, and shuttle to the surface active sites, because of the lower Fermi (E_F) level position and excellent metallic conductivity.[33,34,57] Successfully separated electrons *via* cascade charge transfer contribute to the proton reduction persistently from H_2O with the aid of Pt cocatalyst and NH_2-$Ti_3C_2T_x$. Reserved holes in the $HOMO_{ex}$ of NTU-BDA-THTA are captured by *L*-ascorbic acid, which eventually undergo an oxidation process. In the ternary hybrid, NTU-BDA-THTA (*β*-ketoenamine linkage) and Pt particles serve as the photosensitizer and the co-catalyst for H_2 evolution, respectively. NH_2-$Ti_3C_2T_x$ may be considered as an electron sink and conductor. The generality of covalently bridged 2D/2D COF/NH_2-$Ti_3C_2T_x$ hetero-hybrids for enhanced photocatalytic hydrogen evolution was also clearly demonstrated by the successful application for a series of *β*-ketoenamine-based COFs, including COF-Tp-BDDA, COF-Tp-TAT, FS-COF and COF-Tp-Tt (Figures S59-S64 and associated discussions). Photocatalytic water oxidation on COFs is also challenging for sustainable fuel production from water.[58,59] The HOMO level of NTU-BDA-THTA seems to be suitably positioned for oxidizing water into O_2. Notably, ATNT-4 promotes water oxidation to produce O_2 with an accumulated yield of 2.3 μmol in one hour (Figure S65). The low activity for O_2 evolution might be ascribed to smaller thermodynamic driving force as compared with that of H_2 evolution.[55] These results demonstrate that ATNT-4 could catalyze the reduction or oxidation of water into H_2 or O_2 under the visible light irradiation.

CONCLUSION

We have developed an approach to construct COF-based photocatalyst *via* an integration of linkage evolution and covalent inorganic/organic heterostructure for visible light-induced hydrogen evolution from water. In the present case, the surface area, order degree of structure and light-energy absorption of these pure/mixed linkage COFs are not crucial factors in determining photocatalytic activity. Experimental and theoretical evidence concludes that the increase of HOMO energy with the increase of β-ketoenamine linkage nicely correlates with observed photocatalytic trend. More positively charged potentials of photogenerated holes are easily quenched by sacrificial electron donor to enhance the accessible electron migration for participating in the proton reduction. Meanwhile, the excited state of the mixed-linkage COF may also be suppressed by the imine moiety in NTU-BDA-HTA and NTU-BDA-DHTA to impede the photoredox process. Therefore, our results have demonstrated that the linkages of COFs affect the planar conformation, ordered structure, HOMO energy and excited-state quenching effect, which should be systematically considered to optimize the photocatalytic hydrogen evolution. More importantly, successive artificially coupled heterostructure, guided by covalent connection of inorganic MXene, has been successfully demonstrated. Diverse COF/NH_2-$Ti_3C_2T_x$ hetero-hybrids with sufficient contact interface reveal efficient charge transfer. These covalent hybrids show excellent photocatalytic activity and stability for hydrogen evolution from water as compared to conventional heterostructure counterparts interacted *via* noncovalent interactions such as van der Waals force and hydrogen bonding interaction. This "design-screening-and-reinforce" strategy simultaneously allows the rational construction of COFs and their integration with other functional materials, opening up an avenue for the development of efficient photocatalysts.

ASSOCIATED CONTENT

Supporting Information.

Experimental procedures, characterization data, supplemental figures, and computational details. This material is available free of charge *via* the Internet at http://pubs.acs.org.

AUTHOR INFORMATION

Corresponding Author

*zhaoyanli@ntu.edu.sg

ORCID

Hou Wang: 0000-0002-2066-1856
Cheng Qian: 0000-0002-1392-6975
Dongdong Wang: 0000-0002-6278-0706
Yanli Zhao: 0000-0002-9231-8360

Author Contributions

⊥H. Wang and C. Qian contributed equally to this work.

Notes

The authors declare no competing financial interest.

ACKNOWLEDGMENT

This research is supported by the Singapore Agency for Science, Technology and Research (A*STAR) AME IRG grant (No. A1783c0007) and the Singapore National Research Foundation Investigatorship (No. NRF-NRFI2018-03).

REFERENCES

(1) Diercks, C. S.; Yaghi, O. M. The Atom, the Molecule, and the Covalent Organic Framework. *Science* **2017**, *355*, eaal1585.

(2) Huang, N.; Wang, P.; Jiang, D. Covalent Organic Frameworks: A Materials Platform for Structural and Functional Designs. *Nat. Rev. Mater.* **2016**, *1*, 16068.

(3) Ding, S. Y.; Wang, W. Covalent Organic Frameworks (COFs): From Design to Applications. *Chem. Soc. Rev.* **2013**, *42*, 548-568.

(4) Guan, X.; Li, H.; Ma, Y.; Xue, M.; Fang, Q.; Yan, Y.; Valtchev, V.; Qiu, S. Chemically Stable Polyarylether-Based Covalent Organic Frameworks. *Nat. Chem.* **2019**, *11*, 587-594.

(5) Ma, T.; Kapustin, E. A.; Yin, S. X.; Liang, L.; Zhou, Z.; Niu, J.; Li, L. H.; Wang, Y.; Su, J.; Li, J.; Wang, X.; Wang, W. D.; Wang, W.; Sun, J.; Yaghi, O. M. Single-Crystal X-Ray Diffraction Structures of Covalent Organic Frameworks. *Science* **2018**, *361*, 48-52.

(6) Jin, E.; Asada, M.; Xu, Q.; Dalapati, S.; Addicoat, M. A.; Brady, M. A.; Xu, H.; Nakamura, T.; Heine, T.; Chen, Q.; Jiang, D. Two-Dimensional *sp*² Carbon-Conjugated Covalent Organic Frameworks. *Science* **2017**, *357*, 673-676.

(7) Miao, Z.; Liu, G.; Cui, Y.; Liu, Z.; Li, J.; Han, F; Liu, Y.; Sun X.; Gong, X.; Zhai, Y.; Zhao, Y.; Zeng, Y. A Novel Strategy for the Construction of Covalent Organic Frameworks from Nonporous Covalent Organic Polymers. *Angew. Chem. Int. Ed.* **2019**, *131*, 4960-4964.

(8) Spitler, E. L.; Dichtel, W. R. Lewis Acid-Catalysed Formation of Two-Dimensional Phthalocyanine Covalent Organic Frameworks. *Nat. Chem.* **2010**, *2*, 672-677.

(9) Calik, M.; Auras, F.; Salonen, L. M.; Bader, K.; Grill, I.; Handloser, M.; Medina, D. D.; Dogru, M.; Löbermann, F.; Trauner, D.; Hartschuh, A.; Bein, T. Extraction of Photogenerated Electrons and Holes from a Covalent Organic Framework Integrated Heterojunction. *J. Am. Chem. Soc.* **2014**, *136*, 17802-17807.

(10) Dalapati, S.; Jin, E.; Addicoat, M.; Heine, T.; Jiang, D. Highly Emissive Covalent Organic Frameworks. *J. Am. Chem. Soc.* **2016**, *138*, 5797-5800.

(11) Xu, H.; Gao, J.; Jiang, D. Stable, Crystalline, Porous, Covalent Organic Frameworks as a Platform for Chiral Organocatalysts. *Nat. Chem.* **2015**, *7*, 905-912.

(12) Ming, J.; Liu, A.; Zhao, J.; Zhang, P.; Huang, H.; Lin, H.; Xu, Z.; Zhang, X.; Wang, X.; Hofkens, J.; Roeffaers, M. B. J.; Long, J. Hot π-Electron Tunneling of Metal-Insulator-COF Nanostructures for Efficient Hydrogen Production. *Angew. Chem. Int. Ed.* **2019**, *131*, 18458-18462.

(13) Li, L.; Zhou, Z.; Li, L.; Zhuang, Z.; Bi, J.; Chen, J.; Yu, Y.; Yu, J. Thioether-Functionalized 2D Covalent Organic Framework Featuring Specific Affinity to Au for Photocatalytic Hydrogen Production from Seawater. *ACS Sustain. Chem. Eng.* **2019**, *7*, 18574-18581.

(14) Liu, W.; Li, X.; Wang, C.; Pan, H.; Liu, W.; Wang, K.; Zeng, Q.; Wang, R.; Jiang, J. A Scalable General Synthetic Approach toward Ultrathin Imine-Linked Two-Dimensional Covalent Organic Framework Nanosheets for Photocatalytic CO_2 Reduction. *J. Am. Chem. Soc.* **2019**, *141*, 17431-17440.

(15) Deng, Y.; Zhang, Z.; Du, P.; Ning, X.; Wang, Y.; Zhang, D.; Liu, J.; Zhang, S.; Lu, X. Bridging Ultrasmall Au Clusters into the Pores of a Covalent Organic Framework for Enhanced Photostability and Photocatalytic Performance. *Angew. Chem. Int. Ed.* **2020**, 10.1002/anie.201916154.

(16) Wang, S.; Sun, Q.; Chen, W.; Tang, Y.; Aguila, B.; Pan, Y.; Zheng, A.; Yang, Z.; Wojtas, L.; Ma, S.; Xiao, F. Programming Covalent Organic Frameworks for Photocatalysis: Investigation of Chemical and Structural Variations. *Matter* **2020**, *2*, 416–427.

(17) Huang, W.; He, Q.; Hu, Y.; Li, Y. Molecular Heterostructures of Covalent Triazine Frameworks for Enhanced Photocatalytic Hydrogen Production. *Angew. Chem. Int. Ed.* **2019**, *58*, 8676-8680.

(18) Ascherl, L.; Evans, E. W.; Gorman, J.; Orsborne, S.; Bessinger, D.; Bein, T.; Friend, R. H.; Auras, F. Perylene-Based Covalent Organic Frameworks for Acid Vapor Sensing. *J. Am. Chem. Soc.* **2019**, *141*, 15693-15699.

(19) Zeng Y, Zou R., Luo Z., Zhang H., Yao X., Ma X., Zou R., Zhao Y.; Covalent Organic Frameworks Formed with Two Types of Covalent Bonds Based on Orthogonal Reactions. *J. Am. Chem. Soc.* **2015**, *137*, 1020-1023.

(20) Li, H.; Pan, Q.; Ma, Y.; Guan, X.; Xue, M.; Fang, Q.; Yan, Y.; Valtchev, V.; Qiu, S. Three-Dimensional Covalent Organic Frameworks with Dual Linkages for Bifunctional Cascade Catalysis. *J. Am. Chem. Soc.* **2016**, *138*, 14783-14788.

(21) Qian, C.; Qi, Q.; Jiang, G.; Cui, F.; Tian, Y.; Zhao, Xin. Toward Covalent Organic Frameworks Bearing Three Different Kinds of Pores: The Strategy for Construction and COF-to-COF Transformation *via* Heterogeneous Linker Exchange. *J. Am. Chem. Soc.* **2017**, 139, 6736-6743.

(22) Simon, T.; Bouchonville, N.; Berr, M. J.; Vaneski, A.; Adrović, A.; Volbers, D.; Wyrwich, R.; Döblinger, M.; Susha, A. S.; Rogach, A. L.; Jäckel, F.; Stolarczyk, J. K.; Feldmann, J. Redox Shuttle Mechanism Enhances Photocatalytic H_2 Generation on Ni-Decorated CdS Nanorods. *Nat. Mater.* **2014**, *13*, 1013-1018.

(23) Peng, Y.; Bouchonville, N.; Berr, M. J.; Vaneski, A.; Adrović, A.; Volbers, D.; Wyrwich, R.; Döblinger, M.; Susha, A. S.; Rogach, A. L.; Jäckel, F.; Stolarczyk, J. K.; Feldmann, J. Hybridization of MOFs and COFs: A New Strategy for Construction of MOF@COF Core-Shell Hybrid Materials. *Adv. Mater.* **2018**, *30*,

1705454.
(24) Zhang, F. M.; Sheng, J.; Yang, Z.; Sun, X.; Tang, H.; Lu, M.; Dong, H.; Shen, F.; Liu, J.; Lan, Y. Rational Design of MOF/COF Hybrid Materials for Photocatalytic H_2 Evolution in the Presence of Sacrificial Electron Donors. *Angew. Chem. Int. Ed.* **2018**, *57*, 12106-12110.
(25) Sun, D.; Jang, S.; Yim, S. J.; Ye, L.; Kim, D. P. Metal Doped Core-shell Metal-Organic Frameworks@Covalent Organic Frameworks (MOFs@COFs) Hybrids as a Novel Photocatalytic Platform. *Adv. Funct. Mater.* **2018**, *28*, 1707110.
(26) Yang, S.; Hu, W.; Zhang, X.; He, P.; Pattengale, B.; Liu, C.; Cendejas, M.; Hermans, I.; Zhang, X.; Zhang, J.; Huang, J. 2D Covalent Organic Frameworks as Intrinsic Photocatalysts for Visible Light-Driven CO_2 Reduction. *J. Am. Chem. Soc.* **2018**, *140*, 14614-14618.
(27) Banerjee, T.; Haase, F.; Savasci, G.; Gottschling, K.; Ochsenfeld, C.; Lotsch, B. V. Single-Site Photocatalytic H2 Evolution from Covalent Organic Frameworks with Molecular Cobaloxime Co-Catalysts. *J. Am. Chem. Soc.* **2017**, *139*, 16228-16234.
(28) Zhong, W.; Sa, R.; Li, L.; He, Y.; Li, L.; Bi, J.; Zhuang, Z.; Yu, Y.; Zou, Z. A Covalent Organic Framework Bearing Single Ni Sites as a Synergistic Photocatalyst for Selective Photoreduction of CO_2 to CO. *J. Am. Chem. Soc.* **2019**, *141*, 7615-7621.
(29) Lu, S.; Hu, Y.; Wan, S.; McCaffrey, R.; Jin, Y.; Gu, H.; Zhang, W. Synthesis of Ultrafine and Highly Dispersed Metal Nanoparticles Confined in a Thioether-Containing Covalent Organic Framework and Their Catalytic Applications. *J. Am. Chem. Soc.* **2017**, *139*, 17082-17088.
(30) Thote, J.; Aiyappa, H. B.; Deshpande, A.; Diaz, D. D.; Kurungot, S.; Banerjee, R. A Covalent Organic Framework-Cadmium Sulfide Hybrid as a Prototype Photocatalyst for Visible-Light-Driven Hydrogen Production. *Chem. Eur. J.* **2014**, *20*, 15961-15965.
(31) Wang, H.; Wu, Y.; Yuan, X.; Zeng, G.; Zhou, J.; Wang, X.; Chew J. W. Clay-Inspired MXene-Based Electrochemical Devices and Photo-Electrocatalyst: State-of-the-Art Progresses and Challenges. *Adv. Mater.* **2018**, *30*, 1704561.
(32) Ghidiu, M.; Lukatskaya, M. R.; Zhao, M. Q.; Gogotsi, Y.; Barsoum, M. W. Conductive Two-Dimensional Titanium Carbide 'Clay' with High Volumetric Capacitance. *Nature* **2014**, *516*, 78-81.
(33) Tian, Y.; Que, W.; Luo, Y.; Yang, C.; Yin, X.; Kong, L. B. Surface Nitrogen-Modified 2D Titanium Carbide (MXene) with High Energy Density for Aqueous Supercapacitor Applications. *J. Mater. Chem. A* **2019**, *7*, 5416-5425.
(34) Wen, Y.; Rufford, T. E.; Chen, X.; Li, N.; Lyu, M.; Dai, L.; Wang, L. Nitrogen-Doped $Ti_3C_2T_x$ MXene Electrodes for High-performance Supercapacitors. *Nano Energy* **2017**, *38*, 368-376.
(35) Patterson, A. L. The Scherrer Formula for X-Ray Particle Size Determination. *Phys. Rev.* **1939**, *56*, 978-982.
(36) Vazquez-Molina, D. A.; Pope, G. M.; Ezazi, A. A.; Mendoza-Cortes, J. L.; Harper, J. K.; Uribe-Romo, F. J. Framework *vs*. Side-Chain Amphidynamic Behaviour in Oligo-(Ethylene Oxide) Functionalised Covalent-Organic Frameworks. *Chem. Commun.* **2018**, *54*, 6947-6950.
(37) Vyas, V. S.; Haase, F.; Stegbauer, L.; Savasci, G.; Podjaski, F.; Ochsenfeld C.; Lotsch, B. V. A Tunable Azine Covalent Organic Framework Platform for Visible Light-Induced Hydrogen Generation. *Nat. Commun.* **2015**, *6*, 8508.
(38) Berrones-Reyes, J. C.; Muňoz-Flores, B. M.; Canton-Diaz, A. M.; Treto-Suarez, M. A.; Paez-Hernandez, D.; Schott, E.; Zarate, X.; Jimenez-Perez, V. M. Quantum Chemical Elucidation of the Turn-On Luminescence Mechanism in Two New Schiff Bases as Selective Chemosensors of Zn^{2+}: Synthesis, Theory and Bioimaging Applications. *RSC Adv.* **2019**, *9*, 30778–30789.
(39) Luo, J.; Zhang, W.; Yuan, H.; Jin, C.; Zhang, L.; Huang, H.; Liang, C.; Xia, Y.; Zhang, J.; Gan, Y.; Tao X. Pillared Structure Design of MXene with Ultralarge Interlayer Spacing for High-Performance Lithium-Ion Capacitors. *ACS Nano* **2017**, *11*, 2459-2469.
(40) Anasori, B.; Lukatskaya, M. R.; Gogotsi, Y. 2D Metal Carbides and Nitrides (MXenes) for Energy Storage. *Nat. Rev. Mater.* **2017**, *2*, 16098.
(41) Mashtalir, O.; Naguib, M.; Mochalin, V. N.; Dall'Agnese, Y.; Heon, M.; Barsoum, M. W.; Gogotsi, Y. Intercalation and Delamination of Layered Carbides and Carbonitrides. *Nat. Commun.* **2013**, *4*, 1716.
(42) Azquez-Molina, D. A.; Mohammad-Pour, G. S.; Lee, C.; Logan, M. W.; Duan, X.; Harper, J. K.; Uribe-Romo, F. J., Mechanically Shaped Two-Dimensional Covalent Organic Frameworks Reveal Crystallographic Alignment and Fast Li-Ion Conductivity. *J. Am. Chem. Soc.* **2016**, *138, 31*, 9767-9770.
(43) Sun, B.; Zhu, C.-H.; Liu, Y.; Wang, C.; Wan, L.-J.; Wang, D., Oriented Covalent Organic Framework Film on Graphene for Robust Ambipolar Vertical Organic Field-Effect Transistor. *Chem. Mater.* **2017**, *29*, 4367-4374.
(44) Spitler, E. L.; Colson, J. W.; Uribe-Romo, F. J.; Woll, A. R.; Giovino, M. R.; Saldivar, A.; Dichtel, W. R., Lattice Expansion of Highly Oriented 2D Phthalocyanine Covalent Organic Framework Films. *Angew. Chem. Int. Ed.* **2012**, *124*, 2677-2681.
(45) Colson, J. W.; Woll, A. R.; Mukherjee, A.; Levendorf, M. P.; Spitler, E. L.; Shields, V. B.; Spencer, M. G.; Park, J.; Dichtel, W. R., Oriented 2D Covalent Organic Framework Thin Films on Single-Layer Graphene. *Science* **2011**, *332*, 228-231.
(46) Xu, L.; Zhou, X.; Tian, W. Q.; Gao, T.; Zhang, Y. F.; Lei, S.; Liu, Z. F., Surface-Confined Single-Layer Covalent Organic Framework on Single-Layer Graphene Grown on Copper Foil. *Angew. Chem. Int. Ed.* **2014**, *53,* 9564-9568.
(47) Shchyrba, A.; Wäckerlin, C.; Nowakowski, J.; Nowakowska, S.; Björk, J.; Fatayer, S.; Girovsky, J.; Nijs, T.; Martens, S. C.; Kleibert, A.; Stöhr, M.; Ballav, N.; Jung, T. A.; Gade, L. H. Controlling the Dimensionality of On-Surface Coordination Polymers *via* Endo- or Exoligation. *J. Am. Chem. Soc.* **2014**, *136*, 9355-9363.
(48) Liu, H.; Chu, J.; Yin, Z.; Cai, X.; Zhuang, L.; Deng, H. Covalent Organic Frameworks Linked by Amine Bonding for Concerted Electrochemical Reduction of CO_2. *Chem* **2018**, *4*, 1696-1709.
(49) Nesterov, V. V.; Antipin, M. Y.; Nesterov, V. N.; Penn, B. G.; Frazier, D. O.; Timofeeva, T. V., Thermally Stable Imines as New Potential Nonlinear Optical Materials. *Cryst. Growth Des.* **2004**, *4*, 521-531.
(50) Wang, H.; Sun, Y.; Wu, Y.; Tu, W.; Wu, S.; Yuan, X.; Zeng, G.; Xu, Z.; Li, S.; Chew, J. W. Electrical Promotion of Spatially Photoinduced Charge Separation *via* Interfacial-Built-In Quasi-Alloying Effect in Hierarchical $Zn_2In_2S_5/Ti_3C_2(O,OH)_x$ Hybrids toward Efficient Photocatalytic Hydrogen Evolution and Environmental Remediation. *Appl. Catal. B* **2019**, *245*, 290-301.
(51) Gong, G.; Liu, Y.; Mao, B.; Tan, L.; Yang, Y.; Shi, W. Ag Doping of Zn-In-S Quantum Dots for Photocatalytic Hydrogen Evolution: Simultaneous Bandgap Narrowing and Carrier Lifetime Elongation. *Appl. Catal. B* **2017**, *216*, 11-19.
(52) Ran, J.; Gao, G.; Li, F.; Ma, T.; Du, A.; Qiao, S. Z. Ti_3C_2 MXene Co-Catalyst on Metal Sulfide Photo-Absorbers for Enhanced Visible-Light Photocatalytic Hydrogen Production. *Nat. Commun.* **2017**, *8*, 13907.
(53) Wang, X.; Chen, L.; Chong, S. Y.; Little, M. A.; Wu, Y.; Zhu, W.; Clowes, R.; Yan, Y.; Zwijnenburg, M. A.; Sprick, R. S.; Cooper, A. I. Sulfone-Containing Covalent Organic Frameworks for Photocatalytic Hydrogen Evolution from Water. *Nat. Chem.* **2018**, *10*, 1180-1189.
(54) Bi, S.; Yang, C.; Zhang, W.; Xu, J.; Liu, L.; Wu, D.; Wang, X.; Han, Y.; Liang, Q.; Zhang, F. Two-Dimensional Semiconducting Covalent Organic Frameworks *via* Condensation at Arylmethyl Carbon Atoms. *Nat. Commun.* **2019**, *10*, 2467.
(55) Wei, S.; Zhang, Fan.; Zhang, W.; Qiang, P.; Yu, K.; Fu, X.; Wu, D.; Bi, S.; Zhang, F. Semiconducting 2D Triazine-Cored Covalent Organic Frameworks with Unsubstituted Olefin Linkages. *J. Am. Chem. Soc.* **2019**, *141*, 14272-14279.
(56) Biswal, B. P.; Vignolo-González, H. A.; Banerjee, T.; Grunenberg, L.; Savasci, G.; Gottschling, K.; Nuss, J.; Ochsenfeld, C.; Lotsch, B. V. Sustained Solar H_2 Evolution from a Thiazolo[5,4-d]Thiazole-Bridged Covalent Organic Framework and Nickel-Thiolate Cluster in Water. *J. Am. Chem. Soc.* **2019**, *141*, 11082-

11092.
(57) Sun, L.; Li, R.; Zhan, W.; Yuan, Y.; Wang, X.; Han X.; Zhao, Y. Double-Shelled Hollow Rods Assembled from Nitrogen/Sulfur-Codoped Carbon Coated Indium Oxide Nanoparticles as Excellent Photocatalysts. *Nat. Commun.* **2019***, 10*, 2270.
(58) Jin, E.; Lan, Z.; Jiang, Q.; Geng, K.; Li, G.; Wang, X.; Jiang, D. 2D sp^2 Carbon-Conjugated Covalent Organic Frameworks for Photocatalytic Hydrogen Production from Water. *Chem* **2019**, *5*, 1632-1647.
(59) Chen, J.; Tao, X.; Li, C.; Ma, Y.; Tao, L.; Zheng, D.; Zhu, J.; Li, H.; Li, R.; Yang, Q. Synthesis of Bipyridine-Based Covalent Organic Frameworks for Visible-Light-Driven Photocatalytic Water Oxidation. *Appl. Catal. B* **2020**, *262*, 118271.

Table of Contents artwork here